The abundance of Argon in Tycho's supernova remnant as an indicator of the double-detonation scenario

Luc van de Moosdijk

December 16, 2013

Abstract

An analysis of the Argon concentration in SNR-1572, 'Tycho' has been performed. Based on a Principal Component Analysis (PCA), spectra of regions with high and low argon concentration were taken. I find that the PCA is good indicator of argon presence, and that there are three general regions of argon abundance, all are found near the rim of the remnant, providing evidence for a double detonation. Argon abundances of several orders of magnitude above solar are found, and I conclude that Tycho's SNR is a candidate for the double-detonation scenario.

Contents

Chapter 1

Introduction

This thesis reprents my research into the argon concentration of Tycho's SNR over the past 12 months.

Chapter 2 contains a description of the Chandra telescope its history, and the CCDs used to obtain the data for this thesis. Chapter 3 is a general discussion of which data I have used and results of fits. Chapter 4 contains a discussion of the obtained data. Chapter 5 finally discusses some ways in which this research could be improved. The appendices contain full results for the PCA, a list of important abundancies for all six models used, and a discussion of the method behind PCA.

1.1 General properties of type 1a supernovae

Supernovae are classified as type 1a based on their spectroscopic features. The general category of type 1 indicates that there are no hydrogen absorption lines in the emission spectra, while the -a suffix means that there are strong silicon absorption lines in the spectrum.

The basic physical mechanism for type 1a supernovae is as follows (Hillebrandt and Niemeyer [2000]): A thermonuclear explosion (i.e. the energy originates from explosive nuclear burning, not from gravitational energy during a core collapse) occurs due to matter accreting onto a C/O White Dwarf. This matter produces radioactive ^{56}Ni. This then decays in 8.8 days into ^{56}Co, which in turn decays into ^{56}Fe. This decay chain gives this type of supernova its characteristic light curve (graph of luminosity versus time).

The fact that a type 1a supernova is formed due to matter accretion means that these supernovae can only form in binary systems. This still leaves open the question whether progenitor systems are more likely double degenerate (a white dwarf accreting onto an other white dwarf), or singly degenerate (a main sequence star accreting onto the white dwarf).

By observing distant galaxies, Scannapieco and Bildsten [2005] have found that the expression for total type 1a supernova rate has two components: One

proportional to star formation rate, and one proportional to stellar mass. The first of these terms is more important in young populations, while the second one is dominant in old stellar populations.

Because type 1a supernovae are explosions of C/O white dwarfs, which have masses close to the Chandrasekhar limit (1.38 $M_\odot$), the variation in peak brightness between them is much less than that of type 2 supernovae. This relatively small variation in brightness allows type 1a supernova remants to be used as standard candles.

1.2 Tycho's Supernova Remnant

While much is still uncertain about the progenitor systems of type 1a supernovae,Badenes et al. [2008] have restricted the possible metallicity of Tycho's progenitor to $0.0048^{+0.0051}_{-0.0036}$ ($\log[Z] = -1.32^{+0.67}_{-0.34}$). The uncertainty in this metallicity level is big enough to be compatible with solar metallicity, but it does exclude subsolar values. While being above-average for the galactic region is which Tycho's SNR is found, the metallicity is still within the spread of measured [Fe/H] values. All of this suggests a young progenitor age, of a few Gyr or less.

Previous studies concerned with finding the abundances of certain elements in Tycho's supernova remnant include Hwang and Gotthelf [1997], who, based on *ASCA* measurements, found the abundance of S/Si to be 1.1-1.6 times the solar value, the abundance of Ar/Si to be 0.4-1.3 times the solar value (assuming Ar and Si have the same ionization age), and the abundance of Ca/Si to be between 5 and 30 times the solar amount (again, assuming the same ionization age for both elements.), but it is more likely that much calcium arises from hotter gas associated with the blast wave.

Tamagawa et al. [2009]used *Suzaku* observations of Tycho's supernova remnant to conclude that the ionization of Chromium and Manganese and Iron Kα in the remnant where of ionization 'Ne-like or thereabouts'. While they do not calculate the abundances because the models used to determine abundances based on x-ray emissions under non-equilibrium do not include chromium and manganese, they did include equivalent widths for the lines above 4 keV. They found 9.7 eV for calcium, 23.8 for chromium, 13.7 for manganese, 1.04×10^3 for iron Kα, 70.5 for iron Kβ and 25.1 for nickel.

Decourchelle et al. [2001]used *XMM* measurements to extract the spectrum from three areas in the southwest of the remnant. Using a two-component non-equilibrium model, they found abundances for silicon of between 1.1 and 2.1 solar photospheric abundances, abundances for sulphur of between 2.1 and 4.6 solar photospheric abundances, and iron abundances of between 0.2 and 0.06 solar photospheric abundances.

Hwang et al. [2002]used *Chandra* to identify clumps of silicon spread throughout the remnant. They hypothesized that many of these clumps seen in the interior of the remnant are 'finger-like' appendages stretching out from the edge of the remnant, but seen face on. This would suggest that the clumps of matter

are concentrated more at the rim of the remnant that in the center of it.

Finally, Vancura et al. [1995]looked at a region comparable to my region of high abundance from component 9 (see Chapter 3 on page 10 for more information). They used *Rosat* data and a single-temperature, single-ionization-timescale non-equilibrium ionization plasma model to find a silicon abundance of 5.19, a Sulphur abundance of 11.89, and an argon abundance of 2.43, in units of solar abundance. While this research is almost 20 years old and based on data with a poorer spectral resolution than the data I have used, it is nonetheless an important benchmark against which to judge my measurements, and hence I have included it here.

From all the above it is possible to form a reasonably good mental image of Tycho's supernova remnant. The age of its progenitor as well as the abundance of its intermediate-mass elements and the spatial variation thereof are all described in the papers I have cited in this paragraph. It is with this information in hand that I will outline my research question, though to do that I first need to describe the various models that try to explain the occurence of type 1a supernovae.

1.3 The double-detonation model

According to Nomoto et al. [1984], the main parameter of how a supernova detonation behaves is helium mass accretion rate. As mass accretes onto the white dwarf, the temperature in the accreted shell rises enough to prompt helium burning.

Nomoto et al. identified three regimes of accretion. First there is relatively rapid accretion, $\dot{M} \gtrsim 4 \times 10^{-8}\,\mathrm{M}_\odot\,\mathrm{yr}^{-1}$. In this case, the hydrogen and helium shell flashes are relatively weak, and carbon and oxygen form in the core until the point for carbon ignition is reached. Once that happens, a carbon deflagration supernova occurs.

Then there is relatively slow accretion, $4 \times 10^{-8} > \dot{M}\,(\mathrm{M}_\odot\,\mathrm{yr}^{-1}) \gtrsim 1 \times 10^{-9}$. Here, the helium flash ignited at or near the bottom of the accreted shell is so strong that it not only produces a helium detonation wave moving outward, but also a carbon detonation wave moving inward. Most of the core material is incinerated and the star is 'disrupted completely'.

The third regime is that of slowest accretion, $\dot{M} < 1 \times 10^{-9}\,\mathrm{M}_\odot\,\mathrm{yr}^{-1}$. In this case, only a single detonation wave of helium is formed, under the condition that the C+O core mass is less than $1.1\mathrm{M}_\odot$. If the core is more massive, the central density of the white dwarf reaches the carbon ignition density and a carbon deflagration supernova occurs.

My research focuses on trying to establish whether or not Tycho's supernova remnant was formed by a double detonation. To understand this model for the explosion, I will first have to talk a little about the other models for type 1a supernovae.

There are two different regimes of burning that can occur before a supernova. As the accreted mass ignites, two possible scenarios occur (Hillebrandt and

Niemeyer [2000]). The first is that the overpressure created by the heat of the burning products is high enough for a shockwave to form that ignites the fuel by compressional heating. This shockwave gives rise to a self-sustaining combustion front moving through the star. This is called a detonation. The burning front generally moves supersonically which means the unburned medium does not expand before it is burned.

The other scenario is that the overpressure is too weak. In this case, an equilibrium between heat diffusion and energy generation is reached. The combustion front now consists of a diffusion zone heating up the fuel to burning temperature, followed by a thin burning layer where energy is generated. This is called a deflagration, and it moves subsonically compared to the unburned material.

Models focusing on just one of these methods of burning have some problems, however: The detonation model produces almost no intermediate-mass elements, and the deflagration model overestimates the amount of ^{54}Fe and other neutron-rich Fe-peak isotopes (Khokhlov [1991]). It is therefore that I base my analysis on the double-detonation model. According to this model (Fink et al. [2010]), the accreted helium shell detonates. This detonation then ignites the core by one of two ways: Either directly, in the case of the helium detonation occuring at the interface of the helium shell and the carbon core; or indirectly, where the helium detonation sends shockwaves through the core which converge on the opposite side of the initial detonation site. This point of converge is also the point of ignition of the white dwarf core (Livne and Arnett [1995]).

1.4 The research question: Was Tycho's Supernova remnant formed by a double detonation?

Although the theory behind type 1a supernovae I outlined in section 1.1 above has become widely accepted, questions of the likely progenitor systems (Vink [2012]) and the explosion scenario have not been completely answered. The latter question is the one that I will concern myself with in this thesis.

As described above, the double-detonation scenario involves an initial detonation in an accreted helium shell. This detonation would have its own nucleosynthesis products. Once the core of the white dwarf ignites, these products would be blown away by the explosion and should thus be found at the edge of the suprenova remnant. I would therefore expect to find clumps of intermediate-mass elements, specifically argon, near the rim of the supernova remnant. That is why all the regions I have selected to probe for argon abundance are situated near the edge of the SNR. (See Chapter 3 on page 10 for a description of these regions).

1.4.1 Nucleosynthesis of Argon

Argon is formed from Sulphur by alpha capture. The Sulphur itself is formed by Oxygen burning, as indicated by the following reactions:

$$^{16}_{8}\mathrm{O} + {}^{16}_{8}\mathrm{O} \rightarrow {}^{32}_{16}\mathrm{S}$$

$$^{32}_{16}\mathrm{S} + {}^{4}_{2}\mathrm{He} \rightarrow {}^{36}_{18}\mathrm{Ar}$$

With the Helium being a byproduct of Silicon formation

$$^{16}_{8}\mathrm{O} + {}^{16}_{8}\mathrm{O} \rightarrow {}^{28}_{14}\mathrm{Si} + {}^{4}_{2}\mathrm{He}$$

It is therefore that argon should arise in places where silicon and sulphur are also present.

According to Fink et al. [2010], up to 21% of the accreted Helium shell can turn into intermediate-mass elements during the initial detonation, and up to 10% of that can be Argon. This indicates that the presence of Argon (Along with other intermediate-mass elements) near the rim of the remnant is a predictor of a double-detonation scenario.

Chapter 2

The Chandra X-ray observatory

Because the data used for this thesis has all been collected by the *Chandra* Space Telescope[1] (or CXO), it would be prudent to go into a little detail about the telescope itself.

2.1 History

The CXO was originally called The Advanced X-Ray Astrophysics Facility (or $AXAF$), and was principally designed to be able to resolve the faint background sources.

The name of the project was the idea of the NASA Associate Administrator at the time. He did not want to use the word "telescope" in describing a future program because the American Congress had already approved a telescope recently, the *Hubble Space Telescope*. (Weiskoppf [2010])

The design was initially proposed by Riccardo Giacconi of AS&E in 1976. While the project intitially underwent 3 years of concept design and preliminary analysis, it did not enter its prototyping phase until 1991. The main reasons for this delay were the delays and cost increases of the *Hubble Space Telescope* and the competition faced from other instruments in other branches of astronomy.

The telescope $AXAF$ was renamed *Chandra* in 1998 in honor of astrophysicist Subrahmanyan Chandrasekhar. It was launched on July 23rd, 1999 and was the heaviest payload ever delivered by a Space Shuttle.

[1] For more general information about the mission and the telescope itself, see http://chandra.harvard.edu/index.html

2.2 Design

Among the requirements for the device were a large telescope area, access to the entire sky with more than 85% available at any time, spatially resolved spectroscopy with at least modest ($E/\triangle E \approx 10$ to 50) energy resolution, and the ability to locate the measured photons on the sky. This resolution would allow it to resolve lines which are up to 20 eV apart as distinct, depending on the region of the x-ray spectrum being looked at and the specifics of the detector itself. However, by far the most stringent and crucial requirement was for the telescope to be able to image to better than 0.5" FWHM. More precisely, it was required that a 1" diameter circle about a point source would contain 70%, and 20%, of the photons imaged at 1 and at 8 keV, respectively. This allows high contrast for large dynamic range, and gives an imaging point spread function (PSF) which is not a strong function of energy.(Schwartz [2004])

The telescope consists of two sets of nested cylindrical surfaces, one paraboloid and one hyperboloid. The surfaces themselves consist of 2 cm thick glass substrate with a 330Å thick coating of iridium. The diameters of the mirrors are 65 cm, 87 cm, 99 cm and 123 cm.

The imaging requirement mentioned above was the key to the scientific power of the *Chandra* Observatory. Its imaging capability was a full 100 times better than the previous X-ray missions, *Einstein* and *ROSAT*. This allows Chandra to image jets and outflows in quasars and active galaxies which had previously been considered "point" sources, and to reveal structure and interactions within clusters of galaxies for which the distribution of hot gas had previously been considered smooth and symmetric, and to allow point source detection to fluxes 100 times fainter due to the reduction of the detector area which accumulates background.

2.3 Chips[2]

Chandra is equipped with two Advanced CCD Imaging Spectrometer (ACIS) chips. Each of these contains 10 planar, 1024 x 1024 pixel CCDs; four arranged in a 2x2 array (ACIS-I) used for imaging, and six arranged in a 1x6 array (ACIS-S) used either for imaging or as a grating readout.

A CCD is a solid-state electronic device composed primarily of silicon. A "gate" structure on one surface defines the pixel boundaries by alternating voltages on three electrodes spanning a pixel. The silicon in the active (depletion) region (the region below the gates wherein most of the absorption takes place) has an applied electric field so that charge moves quickly to the gate surface. The gates allow confined charge to be passed down a "bucket brigade" (the buried channel) of pixels in parallel to a serial readout at one edge by appropriately varying ("clocking") the voltages in the gates. When the CCD absorbs an

[2]All the information in this section was sourced from The *Chandra* Proposers' Observatory Guide, taken from http://cxc.harvard.edu/proposer/POG/html/index.html

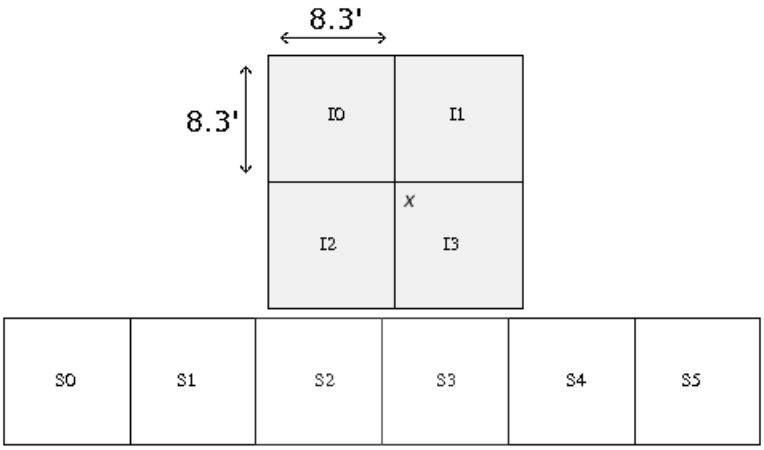

Figure 2.1: The ACIS CCD layout. The 2x2 shaded area represents the I-chips, and the 6x1 area represents the S-chips. The X marks the default aimpoint for the I-chips, in the S-chips it would be in the upper left corner of S3. The two chip areas are not to scale.

x-ray photon, an average of one electron-hole pair is created per 3.7 eV of the photon.

A typical mode of the ACIS CCD operation is: (1) the active region is exposed for a fixed amount of time (full frame $\sim$ 3.2 s); (2) at the end of the exposure, the charge in the active region is quickly ($\sim$ 41 ms) transferred in parallel into the frame store; (3) the next exposure begins; (4) simultaneously, the data in the frame store region is transferred serially to a local processor which, after removing bias, identifies the position and amplitude of any "events" according to a number of criteria depending on the precise operating mode.

The quantum efficiency of the detector depends strongly on the energy of incident photons. In the range I observed for this thesis (1-7.5 keV), the quantum efficiency is between 60 and 90%, see figure 2.2 on the following page.

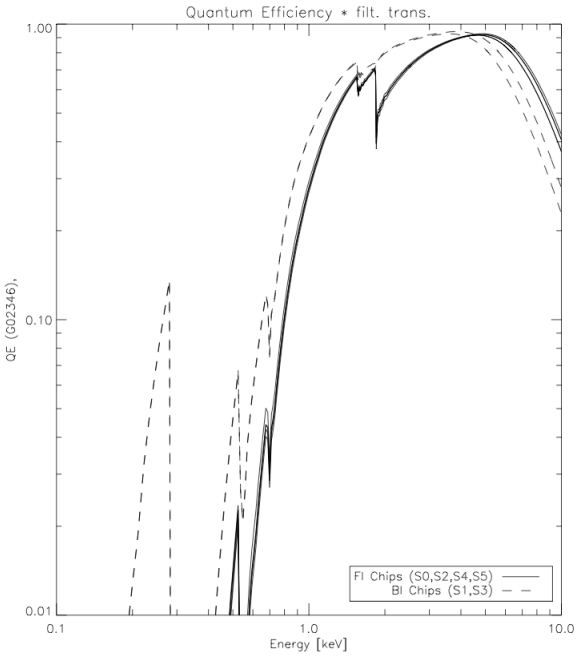

Figure 2.2: The quantum efficiency of the chips, convolved with the transmission of the appropriate optical blocking filter. Fl stands for front-lit, while Bl stands for backlit. The sharp decreases are due to molecular contamination (see text).

The on-board calibration device of the ACIS chips has determined that there is a slow and continuous degradation of the ACIS effective area at low energies. The current explanation is that gas is condensing onto the optical blocking filters of the ACIS due to their lower temperature (the on-board calibration device operates at a higher temperature and shows no such problems) . Gratings observations show that the contaminant is composed of carbon, oxygen and fluorine. In the past it was composed of larger parts oxygen, and before 2002 of mostly carbon. To combat this problem, the *Chandra* team periodically releases models of the contaminant distribution.

Chapter 3

Data analysis

Observations were taken with the ACIS instrument of the Chandra X-ray Observatory. Observation IDs used are 10093-10097. These observations were taken between the 11th and 25th of April 2009 and have a total observation time of 404.5 kiloseconds. This two-week difference is small enough compared to the age of the remnant (around 400 years) to consider the remnant essentially unchanged during the measurement period. The observations were retrieved from the public archive of the Chandra website[1].

Based on a Principal Component Analysis performed by Sjors Broersen (see Appendix A), I identified regions of high Argon concentration in the SNR. Based on these results, I opted to use components 5, 8 and 9 to determine the Argon abundance in the SNR. The first two of those components have a strong positive correlation to Argon abundance, while the last one has a strong negative correlation. Either way, regions of high Argon concentration stand out.

Regions were chosen in such a way that they would have no overlap with other regions, taking into account different components. Because all components are essentially 'slices' of the same SNR, extracting the same region in space from two different components would yield a lot of a redundant data.

Regions were identified with DS9 version 7.2. Spectra were extracted with the `Specextract` script of the CIAO package, version 4.5. I followed the extraction guidelines given by the `Specextract` documentation for extracting the spectrum of an extended source[2]. Spectral fitting was done with the output file[3] in `XSPEC` using a two-plasma non-equilibrium ionization (NEI) model with NEI version 2.0. Because this NEI version does not accurately model the Iron K-line, an additional gauss peak model component was added where appropriate. The goodness of fit was determined with a χ^2statistic, and all the fits have a $\frac{\chi^2}{df}$ of between 1.3 and 1.5 with an average of 408 degrees of freedom. Counts with energy lower than 0.5 keV or higher than 7.0 keV were ignored for the sake of

[1] http://cxc.harvard.edu/cda/public.html

[2] http://cxc.cfa.harvard.edu/ciao/threads/extended/

[3] For a technical explanation of how specextract works and what the output files all mean, see http://cxc.harvard.edu/ciao/ahelp/specextract.html

clarity.

In order to determine how well the PCA predicted the abundance of Argon, I extracted spectra from two regions. One region of high abundance, and one region of low abundance. If the PCA is good indicator of argon abundance, then one would expect the area of high abundance to contain substantially more argon than the region of low abundance.

On the following pages are, sorted by component, the research results: An image indicating the spectrum from the high and low abundance area, an image showing the regions from which the spectra were extracted, and an image of the corresponding principal component. Lastly, there is a tabel indicating the abundances of intermediate-mass elements.

Also included are tables of abundance of intermediate-mass elements for each component. The columns represent areas identified as expected to contain a lot of argon ('high') and those expected to contain much less ('low'), as well as the respective model component, being hot or cold plasma. For the sake of clarity, only abundances of intermediate-mass elements are given here, as well as general parameters (kT, etc.). Errors were computed with `XSPEC`'s `error` command, and all numbers are rounded to two decimal places. Errors that given by a 'less than or equal to' sign are the maximum amount the abundance can deviate from zero without changing the $\chi^2$by more than four points.

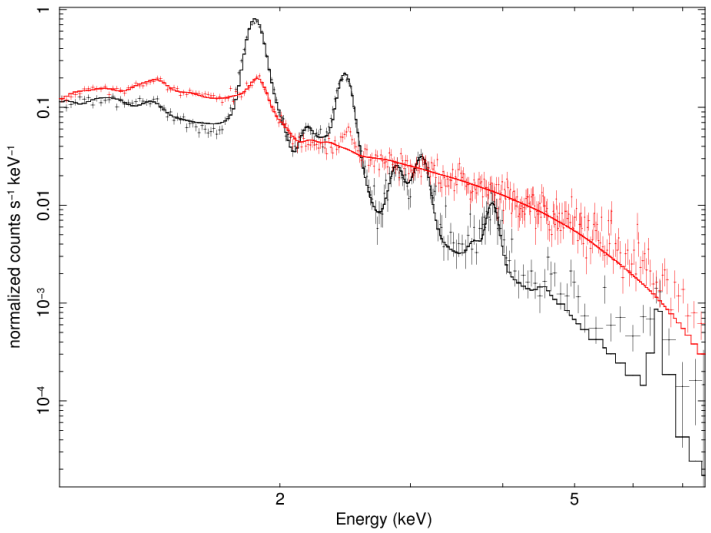

Figure 3.1: Component 5 spectra. Red is the spectrum extracted from the area of low abundance.

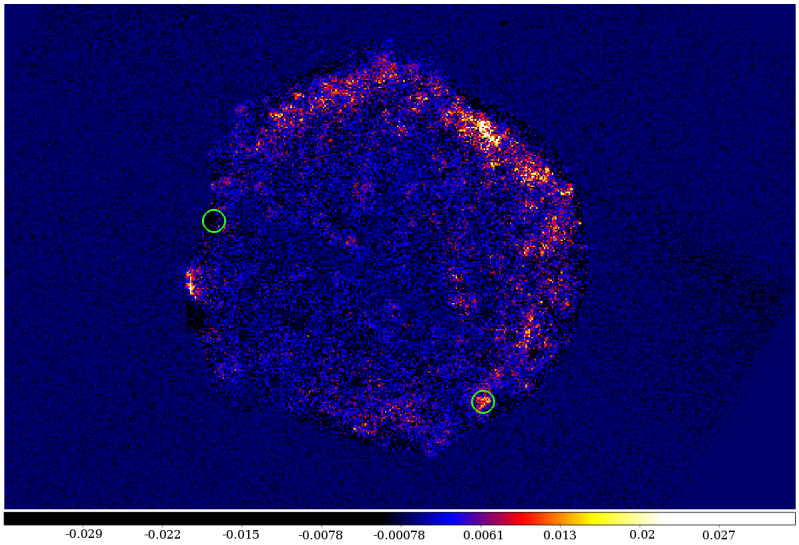

Figure 3.2: Tycho's SNR as observed by *Chandra* and altered with DS9. The color determines the degree to which the concentration lies along component 5 (See B for an explanation). The southeast circle represents the region from which I extracted the spectrum of high argon concentration, while the west circle represents the region from which I extracted the spectrum of low concentration.

Cold plasma	**low**	**high**	**Hot plasma**	**low**	**high**
nH (10^{22})	$1.00^{\pm 0.006}$	$0.87^{\pm 0.01}$			
kT (keV)	$0.86^{\pm 0.01}$	$0.50^{\pm 0.01}$	kT (keV)	$2.55^{\pm 0.06}$	$1.41^{\pm 0.01}$
Si	$82.49^{\pm 30.83}$	$33.19^{\pm 4.49}$	Si	$16.09^{\pm 0.94}$	$12.19^{\pm 0.19}$
S	≤ 2.67	$101.94^{\pm 43.13}$	S	$80.61^{\pm 22.39}$	$19.89^{\pm 0.58}$
Ar	≤ 1.98	$348.02^{\pm 179.81}$	Ar	≤ 1.97	$31.71^{\pm 3.30}$
Ca	≤ 0.89	≤ 1.45	Ca	≤ 1.30	$133.07^{\pm 18.90}$
Fe	$19.65^{\pm 4.44}$	$13.59^{\pm 0.54}$	Fe	$0.11^{\pm 0.05}$	$0.74^{\pm 0.04}$
Ni	$22.88^{519.15}_{-22.88}$	≤ 1.28	Ni	$36.03^{\pm 3.08}$	≤ 1.18
Tau (s/cm^3)	$2.93^{\pm 0.01}$e+09	$6.13^{1.42}_{-1.08}$e+10	Tau (s/cm^3)	$5.72^{\pm 0.06}$e+09	$4.75^{\pm 0.11}$e+10

Table 3.1: Abundances of the regions of component 5, in units of solar abundance

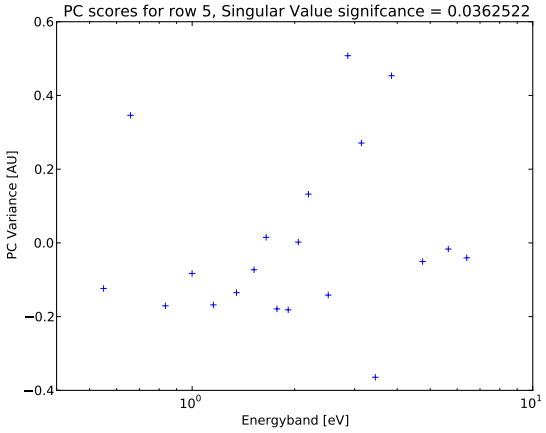

Figure 3.3: Component 5 of the PCA. Note the PC Variance for Argon of about 2.7 (3.1 keV).

The low abundance region is the left one in figure 3.2, while the high abundance region is at the bottom right. The spectrum of the low abundance region is very continuum-like, with no noticeable emission lines past 2.5 keV. The two lines that are present are from silicum and sulphur. This resemblance to a continuum is reflected in the abundances themselves (see appendix A.1), with no noticeable argon present.

The high abundance region has very distinct argon, calcium, silicium and sulphur peaks, all intermediate-mass elements predicted to be present by Fink et al. [2010]. The iron K-line emission peak is very weak, being barely noticeable among the noise. It is thus the only part of the spectrum that is poorly fitted.

Fit characteristics: High abundance region: Reduced χ^2 1.49 with 406 dof. Low abundance region: Reduced χ^2 1.27 with 411 dof.

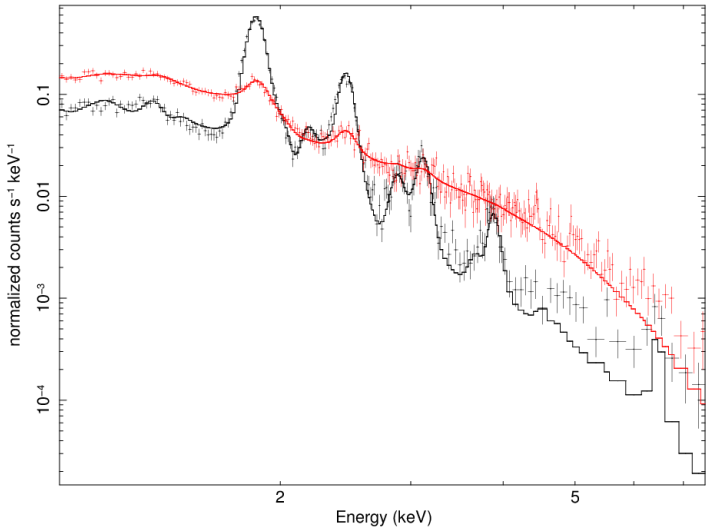

Figure 3.4: Component 8 spectra. Red is the spectrum extracted from the area of low abundance.

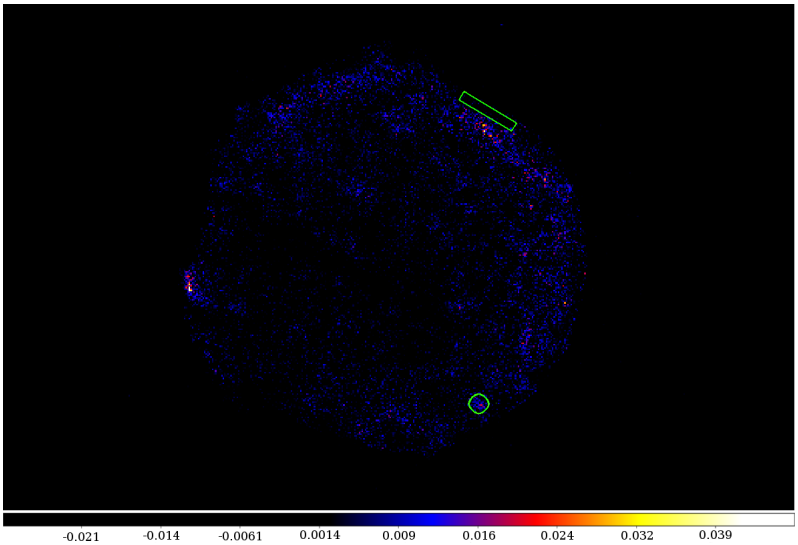

Figure 3.5: *Chandra* in DS9, compared to component 8. The rectangular region is that of low argon concentration. It was chosen in such a way as to examine the edge of the supernova remnant.

Cold plasma	low	high	Hot plasma	low	high
nH (10^{22})	$0.86^{\pm 0.006}$	$0.90^{\pm 0.01}$			
kT (keV)	$0.82^{\pm 0.02}$	$0.59^{\pm 0.00}$	kT (keV)	$1.82^{\pm 0.03}$	$2.46^{\pm 0.07}$
Si	≤ 1.59	$3.40^{\pm 0.19}$	Si	$0.31^{\pm 0.02}$	$361.93^{\pm 8.95}$
S	$3.50^{8.41}_{-3.50}$	$10.90^{\pm 0.65}$	S	$0.67^{\pm 0.07}$	$384.28^{\pm 27.92}$
Ar	$13.24^{23.49}_{-13.24}$	$10.40^{\pm 2.81}$	Ar	$0.85^{4.53}_{-0.85}$	$995.99^{\pm 121.96}$
Ca	$4.41^{84.82}_{-4.41}$	$53.14^{\pm 8.03}$	Ca	$1.03^{\pm 0.67}$	≤ 1.56
Fe	$0.76^{\pm 0.17}$	$0.83^{\pm 0.03}$	Fe	$0.19^{\pm 0.01}$	$1.17^{1.60}_{-1.17}$
Ni	≤ 1.66	≤ 2.07	Ni	$0.36^{\pm 0.11}$	≤ 1.90
Tau (s/cm^3)	$7.72^{\pm 0.44}$e+09	$2.7^{\pm 0.07}$e+13	Tau (s/cm^3)	$3.55^{\pm 0.19}$e+10	$2.85^{\pm 0.09}$e+10

Table 3.2: Abundances of the regions of component 8, in units of solar abundance

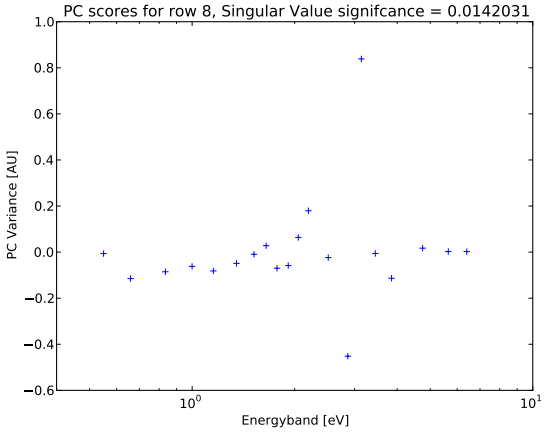

Figure 3.6: Component 8 of the PCA. The PC Variance for Argon is about 8.9 for this component.

Note the extremely high variance in argon abundance accounted for by this component. This means that bright areas in image 3.5 are the areas in the remnant most likely to actually contain argon. This indicates that there might be three general regions of high argon concentration, which suggests further research.

The features notable in the spectra of the previous section once again stand out here. The low abundance region has a mostly continuum-like spectrum, with two faint emission lines, created by silicium and sulphur. The shape of the low abundance region was chosen along the rim of the remnant, to see whether any argon is present outside of places predicted by the PCA, but still in places predicted by the double detonation scenario. That I did not find any argon lines in the low abundance spectrum bodes well for the principal component analysis.

The high abundance region has the same emission lines created by intermediate-mass elements as before. Once again there is a faint iron K-line, see section 4.3 for an analysis.

Fit characteristics: High abundance region: Reduced chisquared 1.62 with 408 degrees of freedom. Low abundance region: Reduced chisquared 1.25 with 409 degrees of freedom.

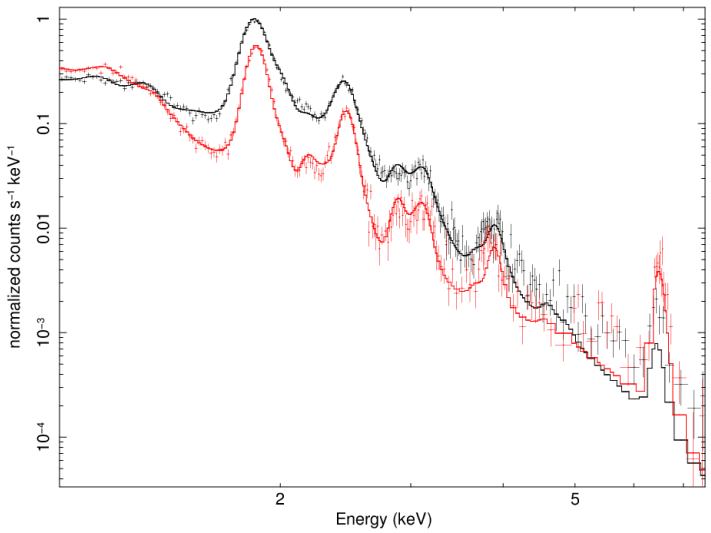

Figure 3.7: Component 9 spectra. Red is the spectrum extracted from the area of low abundance.

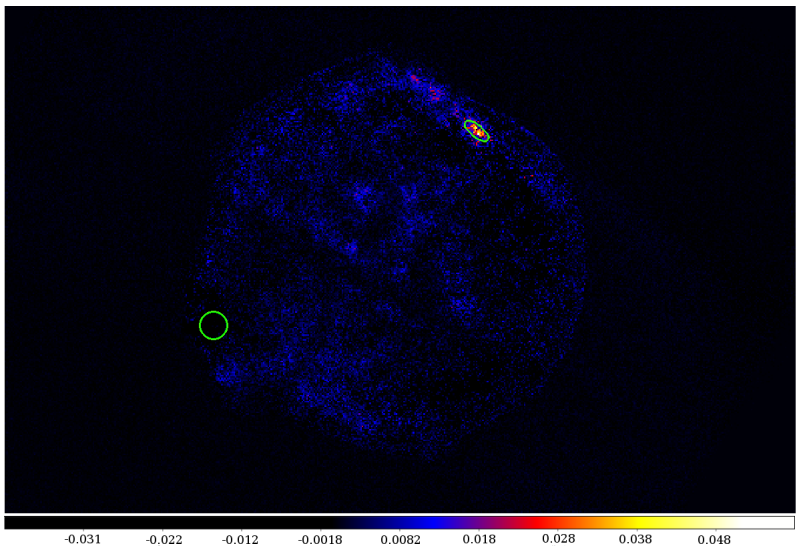

Figure 3.8: *Chandra* imaged in DS9, this time using component 9 as a benchmark. Note that the dark region is the high abundance region in this case, because of the negative correlation between variance and argon abundance in component 9. This means that the southwest region is the region of high abundance, while the northeast region is the region of low abundance. The fact that this region still lights up is due to the fact that it contains a lot of sulphur and silicon, both of which correspond well to component 9.

Cold plasma	low	high	Hot plasma	low	high
nH (10^{22})	$0.83^{\pm 0.03}$	$0.73^{\pm 0.04}$			
kT (keV)	$0.52^{\pm 0.00}$	$0.75^{\pm 0.00}$	kT (keV)	$2.72^{\pm 0.03}$	$16.52^{0.87}_{-1.42}$
Si	$3.42^{\pm 0.21}$	$6.26^{\pm 0.18}$	Si	$155.83^{\pm 3.55}$	$604.76^{\pm 9.59}$
S	≤ 1.64	$32.67^{\pm 2.83}$	S	$267.33^{\pm 9.55}$	$531.17^{\pm 16.87}$
Ar	≤ 1.37	≤ 3.03	Ar	$240.61^{\pm 47.43}$	$455.55^{\pm 57.67}$
Ca	$39.22^{\pm 8.92}$	$188.55^{\pm 8.41}$	Ca	$905.46^{\pm 273.58}$	$691.46^{\pm 117.52}$
Fe	$2.55^{\pm 0.05}$	$1.56^{\pm 0.04}$	Fe	$35.69^{\pm 1.08}$	≤ 1.67
Ni	≤ 1.02	$13.20^{\pm 0.61}$	Ni	≤ 0.98	≤ 2.10
Tau (s/cm^3)	$4.64^{\pm 0.37}$e+13	$3.11^{\pm 0.07}$e+10	Tau (s/cm^3)	$4.49^{\pm 0.06}$e+10	$1.23^{\pm 0.07}$e+10

Table 3.3: Abundances of the regions of component 9, in units of solar abundance

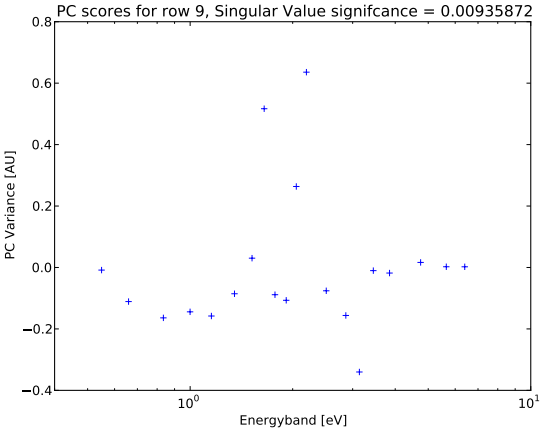

Figure 3.9: Component 9 of the PCA. Note the *negative* value of the PC variance for argon in this component. This means that dark areas are areas of high argon abundance, and light regions are those that contain less argon.

This component presented the greatest challenges to spectral fitting. This reason for this is that while argon has negative correlation, sulphur and silicium have a strong positive correlation. This means that light areas are areas containg little argon but large amounts of sulphur and silicium. Because both these elements are of intermediate mass, theory predicts that (due to their position within the remnant) they both would be formed by the initial shell detonation. It is therefore very unlikely to find a region containing one but not the other. As a result the fits for these regions are the one with the highest uncertainty of all my fits.

The low abundance region confirms this as it has emission lines for all intermediate-mass elements, including a noticeable argon peak. It turns out

that the argon abundance in this region is about half the argon abundance of the high abundance region (See Appendix A.1).

The high abundance region contains all the same lines as the low abundance region, though the argon line is slightly more pronounced, indicating that the correlation identified in figure 3.9 is correct. Note also the pronounced Iron K-line.

Fit characteristics: High abundance region: Reduced chisquared 1.69 with 406 degrees of freedom. Low abundance region: Reduced chisquared 1.59 with 408 degrees of freedom.

Chapter 4

Discussion

4.1 Non-equilibrium ionization

SNR-1572 is named for the year in which it was discovered (It is also called Tycho for its discoverer). This means that the remnant is not even 450 years old, which means that the plasma has only been shocked relatively recently, and each atom has only undergone a few ionizing collisions. This means that the ionizations of the plasma are not yet in equilibrium, some ions will only have lost a few electrons, and while there is enough energy around to ionize them further, they haven't had enough collisions yet to get to a more ionizted state.

Conversely, in collisional ionization equilibrium or CIE, each ion will have undergone a substantial number of collisions, leading to an equilibrium distribution of ionization states. The effect of this NEI is that ionization states of atoms are generally lower than those in CEI (Vink [2012]).

4.2 The iron K-line

All three of my high emission spectra have an emission peak at or around 6.5 keV. This is the so-called iron K-line, and I modeled it seperately in my fits. Originally I did just to improve my fit and because the 2.0 version of the nei model in `XSPEC` seems to ignore it (whereas the 1.0 version modeled the emission peak without problem). This might be because neivers 2.0 does not take K-shell ionization into account when fitting spectra. Nonetheless the specific parameters offered by this model are a useful diagnostic tool for evaluating the ionization in the SNR, which means adding the component to my models provided them with some more explanatory power.

This K-line occurs because an electron from the inner shell (K-shell) of an iron atom is removed. This so-called inner shell ionization is characteristic for plasmas in NEI (Vink [2012]). Once thus ionized, the ion can then either de-excite without radiation, by having an electron from a higher orbital fill the hole, or it can adjust radiatively, which is called fluorescence. The likelihood

Parameter	Component 5	Component 8	Component 9
Line Energy (keV)	6.48	6.46	6.44
Line width (keV)	7.20×10^{-3}	1.89×10^{-6}	1.25×10^{-4}
Norm ($cm^{-2}\,s^{-2}$)	1.25×10^{-6}	5.50×10^{-7}	1.33×10^{-6}

Table 4.1: The strength and position of the iron K-line in the high abundance spectra of each component

for such an adjustment is higher for atoms with larger nuclear charge. Because this transition occurs in the presence of L-shell and M-shell electrons, the effective charge of the nucleus is lower compared to a transition in the helium-like state. As a result the K-line energy rises as a function of ionization state. This means that the position of the K-line in the emission spectrum can be used as a diagnostic tool to estimate the ionization state of the plasma. In table 4.1 below, I summarized my findings. From this data and figure 12 in Vink [2012] I infer that the ion charge of the iron ions in the plasma is as follows: +19 for component 5, and +18 for components 8 and 9. This would put the iron ions at the 'Ne-like or thereabouts' ionization level found by Tamagawa et al. [2009].

The norm (amount of fotons hitting the detector) is a factor 100 smaller than the general norm for my fits, however, which makes any conclusion based on these emission lines suspect. As per Vink [2012], I would ideally need the L-line as well in order to determine the ionization state of the plasma.

The data found byHwang and Gotthelf [1997] for the iron K-line indicates a norm of between 3.9×10^{-4} and 5.0×10^{-4} photons $cm^{-2}\,s^{-2}$, and a line energy of between 6.43 and 6.49 keV.

Tamagawa et al. [2009] found a line width of 1.04 keV for iron Kα, and 70.5 eV for iron Kβ.

4.3 Abundances

My abundances are in certain cases extremely high, and it is hard to fault anything other than a suboptimal fitting method. The literature I've consulted while writing this thesis lists abundances of about 10 times solar at most, which the sole exception being the calcium abundance found by Hwang and Gotthelf [1997]. However they provide an alternate scenario as a more probable cause of the calcium abundance.

Though old, and of poorer resolution, it is especially hard to ignore the work done byVancura et al. [1995]. Looking at an area similar to the one I analyzed in the northwest of the remnant, they found an argon abundance of 2.43, around two orders of magnitude smaller than the abundance I found. While my uncertainties are large, they are by no means substantial enough to explain this difference, and I do not think the difference between *Chandra* and *ROSAT* is enough to explain it either.

4.4 Does the presence of Argon support the delayed-detonation scenario?

From my data it appears that argon is found in modest amounts all throughout the remnant, but is most abundant near the rim in the northwest section of the SNR. That particular spot has high correlation with all three of the components I analyzed, and contains a lot of other intermediate-mass elements as well.

In my models argon and abundance correlated well with silicon abundance (except for component 8), which motivates me to once again point to the results of Hwang et al. [2002]. If the clumps of silicon stretching out from the surface of the remnant do indeed appear all over the SNR, then we could expect to find argon with a similar spatial distribution.

There is however another explanation for the clump of argon found in the northwest. Research by Orlando et al. [2012] indicates that the ejecta might be perturbed by accelerated cosmic rays penetrating the forward shock and leading to clumping. However, this requires very high energies losses to the incident cosmic rays to explain observations in SN 1006. In addition, the compression of the ejecta by accelerated cosmic rays has no significant effect on the growth of Rayleigh-Taylor instabilities, which means that the remnant outline will be only slightly perturbed. This in direct contradiction of observations of Tycho's SNR specifically, because several protrusions of the rim of the remnant have been observed (See, for example, Hwang and Gotthelf [1997]).

In spite of the difference in abundance between my work and those found in literature, I conclude that argon is present in the regions which I have analyzed and show a significant argon abundance. Though the value of the abundance might be off, I do believe that the spatial distribution is correct. This allows me to conclude Tycho's supernova remnant is a candidate for the double-detonation scenario.

Chapter 5

Conclusion

The primary goal of this thesis has been to determine the argon concentration along the rim of Tycho's SNR, and to determine whether this is enough to support the double detonation hypothesis. Along the way I have also verified the accuracy of the performed PCA.

Depending on the region and component, I have found argon abundances that are several hundred times solar, with an error in abundance of around 12%.

Because regions of high argon concentration are only found near the rim of the supernova remnant, and because other intermediate-mass elements predicted by the double-detonation scenario appear alongside the argon, I conclude that the double-detonation is supported by this data.

I suggest that the initial detonation in the helium shell occured somewhere around the northwest part of the white dwarf (using the orientation of the SNR as it is currently). Argon (among other elements) was formed during the shell detonation, then ejected during the core detonation that destroyed the white dwarf.

Based on the fact that I found argon in areas where the PCA indicated argon would be, and I found next to no argon in areas where the PCA indicated little would be, I also conclude that the PCA has served its purpose, it predicted regions of high concentration of a particular element as expected.

5.1 Possible improvements and further research

While I feel my research has been fruitful and the conclusions formed above are supported by the data, there are some things that could have been done better. I used data from component 9 in my research because of its negative relation with argon concentration. I had hoped that looking at the remnant through the lens of this inverse relation would yield interesting structure. As it turned out this was not really the case, but I did end up with a spectrum from the low abundance region filled with emission lines, including one from argon.

The small differences between the high and low abundances in this component weakened my overall conclusion.

The abundances of certain elements seem uncharacteristically high. Follow-up research into this subject would probably first have to reduce some of the abundance numbers here to a more realistic amount.

The iron K-line peak in my models was an ad-hoc addition because the tail end of the spectrum was poorly fit by my two-plasma model and I wanted to improve accuracy. The line diagnostics ended up being too weak to really draw any conclusion and I might have been better off focusing my attention elsewhere. The line itself was also relatively poorly fit and, when compared to literature, produces results outside or at the edge of confidence intervals for iron line diagnostics.

The most obvious avenue of research from here on would be to increase the amount of regions. I have only looked at six distinct regions, while a better conclusion about the double-detonation hypothesis might be formed after the argon concentration of the rim of the SNR has been mapped.

For example, figure 3.5 on page 14 shows a distinct argon spot, which could be more extensively looked at in future research.

Bibliography

The chandra proposers' observatory guide. URL `http://cxc.harvard.edu/proposer/POG/html/index.html`.

C. Badenes, E. Bravo, and J. Hughes. The end of amnesia: A new method for measuring the metallicity of type 1a supernova progenitors using manganese lline in supernova remnants. *The Astrophysical Journal*, 680:L33–L36, 2008.

A. Decourchelle, J.L. Sauvageot, M. Audard, B. Aschebnach, S. Sembay, R. Rothenflug, J. Ballet, T. Stadlbauer, and R.G. West. Xmm-newton observation of the tycho supernova remnant. *Astronomy and Astrophysics*, 365: L218–L224, 2001.

M. Fink, F. K. Röpke, W. Hillebrandt, I. R. Seitenzahl, S. A. Sim, and M. Kromer. Double-detonation sub-chandrasekhar supernovae: Can minimum helium shell masses detonate the core? *Astronomy and Astrophysics*, 514:A53, 2010.

T. J. Gaetz and D. Jerius. *The HRMA User's Guide*, 2005.

W. Hillebrandt and T. Niemeyer. Type ia supernova explosion models. *Annual Review of Astronomy and Astrophysics*, 138:191–230, 2000.

U. Hwang and E. V. Gotthelf. X-ray emission line imaging and spectroscopy of tycho's supernova remnants. *The Astrophysical Journal*, 475:665–682, 1997.

U. Hwang, A. Decourchelle, S. Holt, and R. Petre. Thermal and nonthermal x-ray emission from the forward shock in tycho's supernova remnant. *The Astrophysical Journal*, 581:1101–1115, 2002.

I. T. Jolliffe. *Principal Component Analysis*. Springer, 2002.

A. M. Khokhlov. Delayed detonation model for type 1a supernovae. *Astronomy and Astrophysics*, 245:114–128, 1991.

E. Livne and D. Arnett. Explosions of sub-chandrasekhar mass white dwarfs in two dimension. *The Astrophysical Journal*, 452:62–74, 1995.

K. Nomoto. Accreting white dwarf models for type 1 supernovae. ii. off-center detonation supernovae. *The Astrophysical Journal*, 257:780–792, 1982.

K. Nomoto, F. Thielemann, and K. Yokoi. 1984. *The Astrophysical Journal*, 286:644–658, 1984.

S. Orlando, F. Bocchino, M. Micelo, O. Petruk, and M. L. Pumo. Role of ejecta clumping and back-reaction of accelerated cosmic rays in the evolution of type 1a supernova remnants. *The Astrophysical Journal*, 749:156–168, 2012.

W. H. Press, S. A. Teukolsky, W. T. Vetterling, and B. P. Flannery. *Numerical Recipes: The Art of Scientific Computing*. Cambridge University Press, 2007.

E. Scannapieco and L. Bildsten. The type 1a supernova rate. *The Astrophysical Journal*, 629:L85–L88, 2005.

D. A. Schwartz. The development and scientific impact of the chandra x-ray observatory. *International Journal of Modern Physics*, D13:1239–1248, 2004.

J. Shlens. A tutorial on principal component analysis. published online. URL `http://www.snl.salk.edu/ shlens/pca.pdf`.

T. Tamagawa, A. Hayato, S. Nakamura, Y. Terada, A. Bamba, J. S. Hiraga, J. P. Hughes, U. Hwang, J. Kataoka, K. Kinugasa, H. Kunieda, T. Tanaka, H. Tsunemi, M. Ueno, S. S. Holt, M. Kokubun, E. Miyata, A. Szymkowiak, T. Takahashi, K. Tamura, D. Ueno, and K. Makishima. Suzaku observations of tycho's supernova remnant. *Publications of the Astronomical Society of Japan*, 61:S167–S174, 2009.

O. Vancura, P. Gorenstein, and J. Hughes. Evidence for the elemental variation in the ejecta of the tycho supernova remnant. *The Astrophysical Journal*, 441: 680–688, 1995.

J. Vink. Supernova remnants: The -ray perspective. *Astronomy and Astrophysics Reviews*, 20:49, 2012.

M. C. Weiskoppf. The making of the chandra x-ray observatory: the project scientist's perspective. *Proceedings of the National Academy of Sciences of the United States of America*, 107:7135–7140, 2010.

Appendix A

Full results of the Principal Component Analysis

The results of the PCA are reproduced below. This analysis was originally performed in december of 2011 by Sjors Broersen using a Python script.

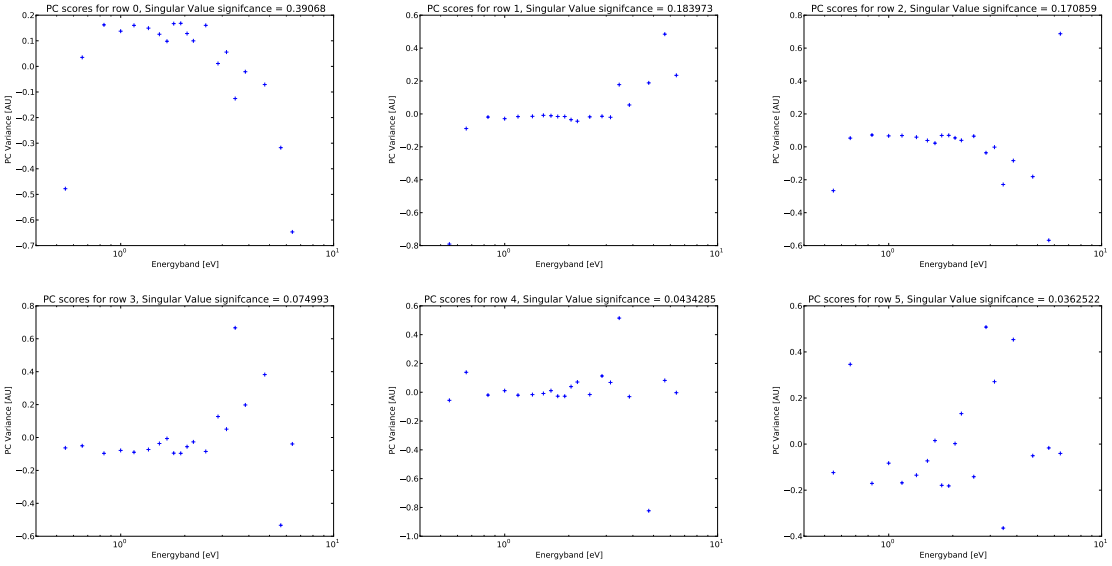

Figure A.1: Results of the PCA, rows 0-6

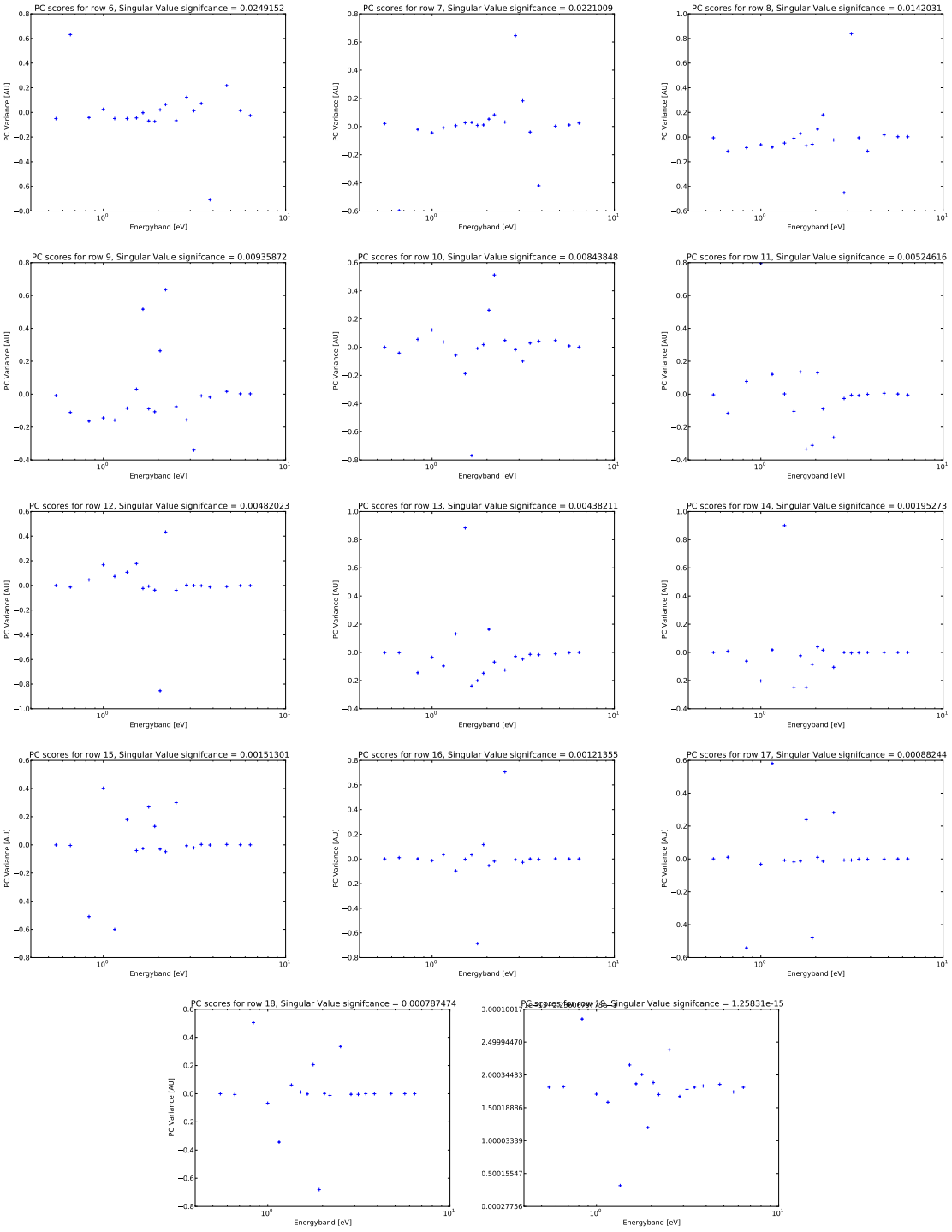

Figure A.2: Results of the PCA, rows 7-19

Appendix B

Principal Component Analysis

B.1 Introduction

Principal Component Analysis (PCA) is a mainstay of modern data analysis. It was first introduced by Pearson (1901), and developed independently by Hotelling in 1933.

The central idea of PCA is to reduce the dimensionality of a data set in which there are a large number of interrelated variables, while retaining as much as possible of the variation present in the data set. This is achieved by transforming to a new set of variables, the principal components (PCs), which are uncorrelated, and which are ordered so that the first few retain most of the variation present in all of the original variables.

In this chapter I will derive the method by which PCA works fairly straightforwardly using eigenvectors. There is another way which is more algebraic and involves *Singular Value Decomposition* (SVD). Though it and PCA are closely linked, I have omitted a derivation based SVD in this thesis.

B.2 A simple example

To understand how PCA works, let us consider the following example: A ball of mass m attached to a massless ideal spring is free to move frictionlessly across a surface (See figure B.1 on the following page). The ball is released a certain distance from equilibrium, and, because the surface and spring are ideal, will oscillate about the equilibrium indefinitely. Intuitively it will be clear that the motion of the ball is dependent on only one variable: the distance from equilibrium (say, x).

Now, being the ignorant[1] researchers that we are, do not know this before-

[1] 'Ignorant' in this case meaning 'having no a priori knowledge of the results of our mea-

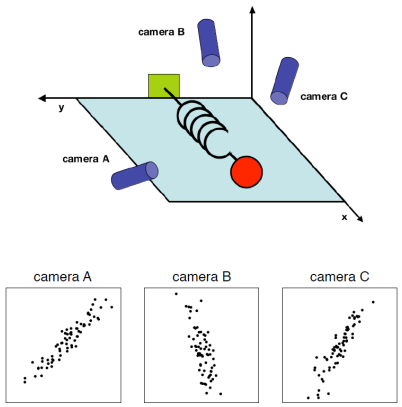

Figure B.1: A ball attached to an oscillating spring, tracked by cameras A, B and C. The lower three images give the position of the ball as tracked by each camera.

hand. We decide to measure the position of the ball in three dimensions, using three cameras, A, B and C. However, due to our ignorance, we are forced to choose three arbitrary positions for the cameras ($\overrightarrow{\mathbf{a}}$, $\overrightarrow{\mathbf{b}}$ and $\overrightarrow{\mathbf{c}}$). Supposing each camera records the position of the ball several times per second, and letting the cameras record for several minutes, we would end up with a cloud of data similar to the one at the bottom of figure B.1 on page 30.

The question is: How do we get from this cloud of naive measurements to a simple equation of x?[2]

Now, let us treat every time sample (or time trial) as an individual sample in our data set. At each point in time, camera A records the position of the ball as (x_A,y_A), camera B records the position as (x_B,y_B), and camera C records the position as (x_C,y_C). Therefore each individual sample can be written as

$$\overrightarrow{X} = \begin{bmatrix} x_A \\ y_A \\ x_B \\ y_B \\ x_C \\ y_C \end{bmatrix}$$

In other words, and more generally: Each sample is a vector that lies in an m-dimensional vector space, where m is the number of measurement types (6 in our example).

surement'.

[2]Obviously, for this example, we would have just measured the experiment along the x-axis with a single camera, but in the real world we often do not know which measurements best reflect the dynamics of the system in question.

The naive basis for this this vector space is then simply

$$\mathbf{B} = \begin{bmatrix} \mathbf{b_1} \\ \mathbf{b_2} \\ \vdots \\ \mathbf{b_m} \end{bmatrix} = \begin{bmatrix} 1 & 0 & \cdots & 0 \\ 0 & 1 & \cdots & 0 \\ \vdots & \vdots & \ddots & \vdots \\ 0 & 0 & \cdots & 1 \end{bmatrix} \equiv \mathbf{I}$$

With this in mind we may now state what PCA asks: Is there another basis, which is a linear combination of the original basis, that *best re-expresses* our data set? Implicitly, the goal is that this new basis will filter out the noise and reveal hidden structures in the data. In our example, the explicit goal of PCA is to determine that the dynamics of the system are along the x-axis (i.e. that the basis of our data is simply $\hat{\mathbf{x}}$)

Let $\mathbf{X}$ be the original data set. Let $\mathbf{Y}$ the new representation of our data (after PCA)[3]. Then, $\mathbf{X}$ and $\mathbf{Y}$ are related by

$$\mathbf{PX} = \mathbf{Y} \tag{B.1}$$

where $\mathbf{P}$ is the transformation we are looking for.

By assuming linearity, the problem reduces to finding the appropriate change of basis. The row vectors $\{\mathbf{p_1}, \ldots, \mathbf{p_m}\}$ in the transformation will become the principal components of $\mathbf{X}$. By asking ourselves "What features do we want $\mathbf{Y}$ to exhibit?" we can begin to think about what properties $\mathbf{P}$ should have.

When trying to best express data, the first step is to reduce noise as much as possible. The amount of noise in a system is dependant on signal strength, and can be expressed through the *signal-to-noise-ratio* (SNR). One way to express this SNR is by the ratio of variances:

$$SNR = \frac{\sigma^2_{signal}}{\sigma^2_{noise}}$$

By defining our SNR this way, we tacitly assume that the direction of largest variance is the most interesting one of our data, and that is indeed one of the assumptions behind PCA (See section B.2.3 on page 34).

See figure B.2 on the next page. The above assumption suggests that the basis for the data in this image is not $\hat{\mathbf{x}_A} = (1, 0)$, or $\hat{\mathbf{y}_A} = (0, 1)$, but the direction along the axis of the cloud. Thus, the dynamics of interest lie along the directions of highest variance and presumably highest SNR. Another thing to note from the image is that we did not really have to record 2 variables. Because of the high amount of covariance between the signal and the noise we can just express one as a function of the other, meaning we only need a single variable to describe the data.

In the 2-dimensional case, covariance can be estimated by looking at the slope of the best-fit line and judging the quality of the fit. For an arbitrary number of dimensions, the procedure is as follows.

[3] $\mathbf{X}$ and$\mathbf{Y}$ are $m \times n$ matrices, where n is the number of samples taken. $\mathbf{P}$ is an $n \times m$ matrix.

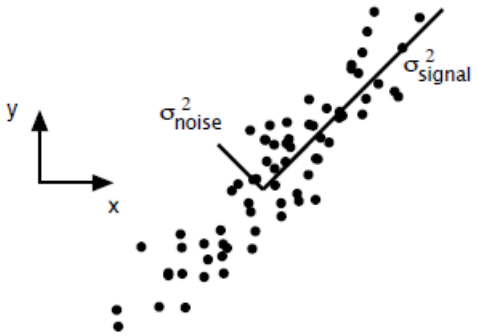

Figure B.2: Simulated data of camera A, with the variances σ^2_{signal} and σ^2_{noise} indicated. Note that the line of largest variance lies not along the basis of the data but along the best-fit line.

B.2.1 Covariance

Consider two sets of measurements with zero means, $A = \{a_1, a_2, \ldots, a_n\}$, $B = \{b_1, b_2, \ldots, b_n\}$. The variance of A and B are individually defined as

$$\begin{aligned} \sigma_A^2 &\equiv \frac{1}{n}\sum_i a_i^2 \\ \sigma_B^2 &\equiv \frac{1}{n}\sum_i b_i^2. \end{aligned}$$

Straightforwardly, the covariance of A and B is then

$$\sigma_{AB}^2 = \frac{1}{n}\sum_i a_i b_i.$$

If we write A and B as vectors,

$$\begin{aligned} \mathbf{a} &= \{a_1, a_2, \ldots, a_n\} \\ \mathbf{b} &= \{b_1, b_2, \ldots, b_n\} \end{aligned}$$

we can express the covariance as a dot product:

$$\sigma_{\mathbf{ab}}^2 = \frac{1}{n}\mathbf{a}\mathbf{b}^T.$$

For an arbitrary number of vectors, the covariance thus becomes

$$\mathbf{C_X} = \frac{1}{n}\mathbf{X}\mathbf{X}^T,$$

with $\mathbf{C_X}$ the covariance matrix, and

$$\mathbf{X} = \begin{bmatrix} x_1 \\ \vdots \\ x_m \end{bmatrix}$$

where each row of $\mathbf{X}$ corresponds to a particular measurement type.

In $\mathbf{C_X}$ diagonal terms represent the variance between measurements, and off-diagonal terms represent the covariance between measurements. Therefore, an ideal version of $\mathbf{C_X}$ would be a diagonal matrix, and would have each succesive diagonal value be ordered according to decreasing variance. The last part would allow us to quantify how "principal" each basis vector would be.

B.2.2 Solving PCA using eigenvector decomposition

Let $\mathbf{C_Y}$ be some manipulation of the covariance matrix in such a way that it has minimized redundancy and a maximized signal. Then

$$\begin{aligned} \mathbf{C_Y} &= \frac{1}{n}\mathbf{Y}\mathbf{Y}^T \\ &= \frac{1}{n}(\mathbf{P}\mathbf{X})(\mathbf{P}\mathbf{X})^T \\ &= \frac{1}{n}\mathbf{P}\mathbf{X}\mathbf{X}^T\mathbf{P}^T \\ &= \mathbf{P}\frac{1}{n}(\mathbf{X}\mathbf{X}^T)\mathbf{P}^T \\ &= \mathbf{P}\mathbf{C_X}\mathbf{P}^T \end{aligned}$$

For any symmetric matrix $\mathbf{A}$ we can write $\mathbf{A} = \mathbf{E}\mathbf{D}\mathbf{E}^T$, where $\mathbf{D}$ is a diagonal matrix, and $\mathbf{E}$ is a matrix of eigenvectors of $\mathbf{A}$ arranged as columns.

If we select $\mathbf{P}$ to be a matrix where each row $\mathbf{p_i}$ is an eigenvector of $\frac{1}{n}\mathbf{X}\mathbf{X}^T$, we have $\mathbf{P} = \mathbf{E}^T$. With this and the fact that for an orthogonal matrix, $\mathbf{P}^{-1} = \mathbf{P}^T$, we can finish evaluating $\mathbf{C_Y}$:

$$\begin{aligned} \mathbf{C_Y} &= \mathbf{P}\mathbf{C_X}\mathbf{P}^T \\ &= \mathbf{P}(\mathbf{E}^T\mathbf{D}\mathbf{E})\mathbf{P}^T \\ &= \mathbf{P}(\mathbf{P}^T\mathbf{D}\mathbf{P})\mathbf{P}^T \\ &= (\mathbf{P}\mathbf{P}^T)\mathbf{D}(\mathbf{P}\mathbf{P}^T) \\ &= (\mathbf{P}\mathbf{P}^{-1})\mathbf{D}(\mathbf{P}\mathbf{P}^{-1}) \\ &= \mathbf{D} \end{aligned}$$

We see that our choice of $\mathbf{P}$ diagonalizes $\mathbf{C_Y}$. We can now conclude:

- The principal components of $\mathbf{X}$ are the eigenvectors of $\mathbf{C_X} = \frac{1}{n}\mathbf{X}\mathbf{X}^T$;
- The i^{th} diagonal value of $\mathbf{C_Y}$ is the variance of $\mathbf{X}$ along $\mathbf{p_i}$

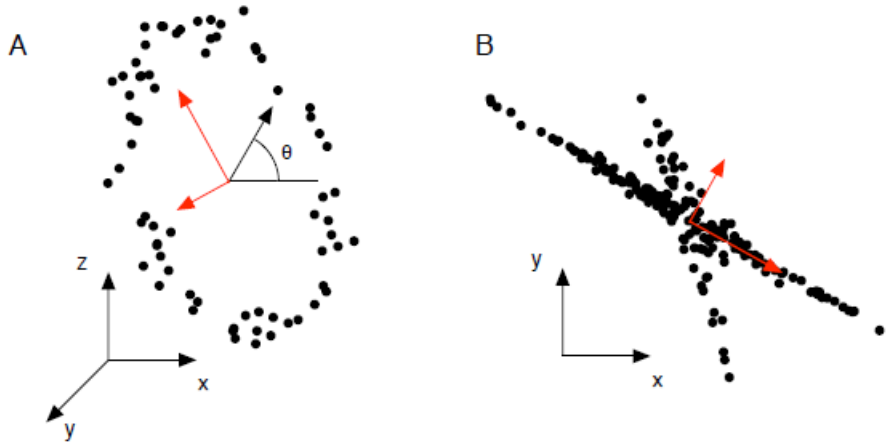

Figure B.3: Two examples of when PCA fails. *A*: A person on a ferris wheel. *B*: Data distributed along non-orthogonal axes. The bases which PCA would pick are given in red.

B.2.3 Summary of assumptions and discussion

The assumptions behind PCA are as follows:

1. PCA is a linear transformation. This way, using PCA becomes a straightforward change of basis.

2. Large variances have important structure. By this assumption, a large variance means a large SNR. Hence, principal components with low variance are assumed to be noise. This is a particularly strong assumption, see below.

3. The principal components are orthogonal. This allows us to solve PCA as in Section B.2.2 above.

The primary benefit of PCA comes from quantifying the importance of each dimension for describing the variability of a data set. In particular, the measurement of the variance along each principle component provides a means for comparing the relative importance of each dimension. Implicitly, the hope is that the variance among a small number of components provides a reasonable characterization of the complete data set.

In the example of the spring, PCA identifies that a majority of variation exists along a single dimension (the direction of motion), even though 6 dimensions are recorded.

Altough PCA works on a multitude of real world problems (See Joliffe chapter 4), there are times when it fails. Figure B.3 *A* shows the dynamics of a person sitting in a ferris wheel. The dynamics of this system can be described by the phase of the wheel, θ. This is a nonlinear combination of the naive basis

(polar coordinates versus cartesian ones), which makes PCA fail. Figure B.3 *B* shows data distributed along non-orthogonal axes. Because PCA always picks a orthogonal base, it doesn't know what to do with the 2nd axis of the data and subsequently breaks down.